

Structural Properties of AMP-activated Protein Kinase DIMERIZATION, MOLECULAR SHAPE, AND CHANGES UPON LIGAND BINDING^{*[3]}

Received for publication, October 9, 2007, and in revised form, February 25, 2008 Published, JBC Papers in Press, March 27, 2008, DOI 10.1074/jbc.M708379200

Uwe Riek^{†,‡,§}, Roland Scholz[‡], Peter Konarev^{¶||}, Arne Rufer^{**}, Marianne Suter[‡], Alexis Nazabal^{††}, Philippe Ringler^{§§}, Mohamed Chami^{§§}, Shirley A. Müller^{§§}, Dietbert Neumann[‡], Michael Forstner^{¶¶}, Michael Hennig^{**}, Renato Zenobi^{††}, Andreas Engel^{§§}, Dmitri Svergun^{¶¶}, Uwe Schlattner^{†,‡,§}, and Theo Wallimann^{†,‡,§}

From the [†]Institute of Cell Biology, and the ^{††}Department of Analytical Chemistry, Laboratory of Organic Chemistry, ETH Zurich, 8093 Zurich, Switzerland, [§]INSERM, U884, Laboratory of Fundamental and Applied Bioenergetics, University Joseph Fourier, Grenoble, France, [¶]EMBL, DESY, 22603 Hamburg, Germany, and ^{||}Institute of Crystallography, Russian Academy of Sciences, 11733 Moscow, Russia, ^{**}F. Hoffmann-La Roche AG, Pharma Research Discovery Chemistry, 4070 Basel, Switzerland, the ^{§§}M. E. Müller Institute for Structural Biology, University of Basel, 4056 Basel, Switzerland, and the ^{¶¶}Zürich Financial Services, 8002 Zurich, Switzerland

Heterotrimeric AMP-activated protein kinase (AMPK) is crucial for energy homeostasis of eukaryotic cells and organisms. Here we report on (i) bacterial expression of untagged mammalian AMPK isoform combinations, all containing γ_1 , (ii) an automated four-dimensional purification protocol, and (iii) biophysical characterization of AMPK heterotrimers by small angle x-ray scattering in solution (SAXS), transmission and scanning transmission electron microscopy (TEM, STEM), and mass spectrometry (MS). AMPK in solution at low concentrations (< 1 mg/ml) largely consisted of individual heterotrimers in TEM analysis, revealed a precise 1:1:1 stoichiometry of the three subunits in MS, and behaved as an ideal solution in SAXS. At higher AMPK concentrations, SAXS revealed concentration-dependent, reversible dimerization of AMPK heterotrimers and formation of higher oligomers, also confirmed by STEM mass measurements. Single particle reconstruction and averaging by SAXS and TEM, respectively, revealed similar elongated, flat AMPK particles with protrusions and an indentation. In the lower AMPK concentration range, addition of AMP resulted in a significant decrease of the radius of gyration by $\sim 5\%$ in SAXS, which indicates a conformational switch in AMPK induced by ligand binding. We propose a structural model involving a ligand-induced relative movement of the kinase domain resulting in a more compact heterotrimer and a conformational

change in the kinase domain that protects AMPK from dephosphorylation of Thr¹⁷², thus positively affecting AMPK activity.

Mammalian AMP-activated protein kinase (AMPK)⁴ and its orthologs found in yeast, plants, insects, invertebrates, and vertebrates are fuel sensors of the eukaryotic cell and function as master regulators of energy metabolism (1–5). AMPK is a serine/threonine protein kinase, consisting of one catalytic α and two regulatory subunits (β and γ), that exist as multiple isoforms ($\alpha_1, \alpha_2, \beta_1, \beta_2, \gamma_1, \gamma_2, \gamma_3$) and splice variants (γ_2 and γ_3), thus allowing for the generation of multiple heterotrimeric isoform combinations. Critical for activation of AMPK is its phosphorylation at Thr¹⁷² in the kinase domain of the α -subunit by either of the two upstream kinases of AMPK, LKB1-MO25 α -STRAD α or Ca²⁺/calmodulin-dependent protein kinase kinase β (CaMKK β) (6–10). In addition, AMP allosterically stimulates AMPK (10, 11) by binding to two pairs of CBS domains in the γ -subunits, called Bateman domains (12). These domains were reported to show high affinity for AMP (10, 13) and lower affinity for ATP (12), although a recent study indicates that these affinities may be similar (14). AMP is a very sensitive signal for an altered cellular energy status (13, 15, 16). Its intracellular concentration changes by 1 order of magnitude upon a 1% change in the cellular ATP concentration, due to the equilibrium reactions of adenylate kinase and creatine kinase (5, 15–18). The latter uses phosphocreatine to rapidly rephosphorylate ADP to ATP and thus maintains a high ATP/ADP ratio (17, 18). Allosteric stimulation of AMPK by AMP increases phosphorylation at Thr¹⁷² and simultaneously inhibits dephosphorylation of this site by protein phosphatase 2C α , thus decreasing the rate of AMPK inactivation (10, 19). The

* This work was supported in part by European Union (EU) FP6 contract LSHM-CT-2004-005272 (EXGENESIS) and Swiss National Science Foundation (NSF) Grants 3100AO-102075 (to T. W. and U. S.), 3100+0-11437/1 (to T. W. and D. N.), and 501 221 (to A. E.); the French Agence Nationale de Recherche (ANR) "chaire d'excellence" (to U. S.); a graduate training fellowship from ETH Zurich (to U. S. and T. W.); a grant from the French Ministry of Education and Research (U. S.); EU Design Study SAXIER Contract 011934 (to D. S. and P. K.); and the Maurice E. Müller Foundation of Switzerland (to A. E.). The costs of publication of this article were defrayed in part by the payment of page charges. This article must therefore be hereby marked "advertisement" in accordance with 18 U.S.C. Section 1734 solely to indicate this fact.

[3] The on-line version of this article (available at <http://www.jbc.org>) contains supplemental Figs. S1 and S2.

¹ Both authors are considered senior authors.

² To whom correspondence may be addressed: INSERM, U884, Laboratory of Fundamental and Applied Bioenergetics, University Joseph Fourier, BP 53, F-38041 Grenoble Cedex 9, France. E-mail: uwe.schlattner@ujf-grenoble.fr.

³ To whom correspondence may be addressed: Inst. of Cell Biology, ETH Zurich, Schafmattstrasse 18, 8093 Zurich, Switzerland. E-mail: theo.wallimann@cell.biol.ethz.ch.

⁴ The abbreviations used are: AMPK, AMP-activated protein kinase; CaMKK, Ca²⁺/calmodulin-dependent protein kinase kinase; CBS, cystathionine β synthase; HPLC, high pressure liquid chromatography; IMAC, immobilized metal ion affinity chromatography; ITC, isothermal titration calorimetry; LKB1, serine/threonine kinase 11 (STK11); MALDI-TOF, matrix-assisted laser desorption ionization-time of flight; MO25, mouse protein 25; MS, mass spectrometry; RS, regulatory sequence; SAMS, synthetic peptide HMR-SAMSGHLVKKRR; SAXS, small angle x-ray scattering; SNF1, carbon catabolite-derepressing protein kinase; STEM, scanning transmission electron microscopy; STRAD, STE20-related adaptor protein; TEM, transmission electron microscopy; Ni-IDA, nickel iminodiacetic acid resin.

Structural Properties of AMPK

precise function of the AMPK β -subunit is not entirely clear. It contains α and γ interaction domains (20, 21), a glycogen-binding domain (22, 23), and β_1 additionally has an N-terminal myristoylation site that may target AMPK to membranes (24). More recently, mutations of Ser¹⁰⁸, an autophosphorylation site, have involved the β -subunit in the allosteric activation mechanism of AMPK (73).

Cellular energy stress and other signals activate AMPK by various pathways, leading as a main consequence to compensatory measures that increase ATP generation and decrease ATP consumption (16). However, the AMPK signaling pathway has not only been implicated in cellular energy homeostasis (13, 25), but also in the regulation of whole body energy balance (2, 26, 27), and more recently in energy-dependent regulation of cell shape (4) and cancer signaling (28–32). The latter is mainly due to the tumor suppressor properties of the upstream kinase LKB1 (6, 8) and the downstream link to signaling by the mammalian target of rapamycin, which is involved in proliferation control (33). Mutations in the AMPK γ -subunit cause several pathologies, mainly due to accumulation of cellular glycogen (34–36). Its multiple downstream effects, including lowering of blood glucose levels, have identified AMPK as a promising target to treat type II diabetes mellitus and the metabolic syndrome (37).

More detailed structural information about mammalian heterotrimeric AMPK is needed to understand its complex molecular architecture and function. Valuable but limited insight has been provided by x-ray structures of isolated AMPK domains: the catalytic domain of the human α_2 -subunit (Protein Data Bank code 2H6D) and its yeast ortholog Snf1 (38, 39), the glycogen-binding domain of the rat β -subunit (40), the Bateman domain of the γ -subunit yeast ortholog Snf4 (41), and a CBS_{3–4}-domain pair of the human γ -subunit (42). More informative, but still limited in their explanatory power, are the recent x-ray structures of truncated versions of a mammalian AMPK complex (14) and its yeast orthologs of *Schizosaccharomyces pombe* (43) and *Saccharomyces cerevisiae* (44) (supplemental Fig. S1). For successful crystallization, large truncations were introduced into the mammalian α - and β -subunits or their yeast homologs. The published core structures all lack the α -subunit kinase domain and a more or less large N-terminal part of the β -subunit. In the *S. pombe* and mammalian structures, almost 50% of the entire complex is missing. The *S. cerevisiae* structure (supplemental Fig. S1) is somewhat less truncated and contains a regulatory sequence (RS, α -subunit) and the glycogen-binding domain (β -subunit).

A major contribution of these structures is the exact definition of subunit interactions. They confirm the structural consensus model of AMPK that had been challenged before (20, 21). In addition, the larger *S. cerevisiae* structure reveals novel interactions of the γ -subunit homologue with both the regulatory domain (α -subunit) and the glycogen-binding domain (β -subunit). The structures also identify the precise nucleotide binding sites on the γ -subunit (see also Fig. 9B). Although in yeast only a single AMP (or ATP) molecule is bound to the γ -homolog (43, 44), probably because yeast AMPK is not activated by AMP, the mammalian AMPK γ -subunit revealed three nucleotide binding sites (14). One site, corresponding to the

yeast binding site, contains a non-exchangeable, fixed AMP, whereas the other two allow for ATP/AMP exchange and thus provide the AMP sensor function of AMPK. However, neither of the AMP-containing AMPK core structures showed an appreciable structural difference as compared with ATP-containing or nucleotide-free structures. This observation and the absence of the kinase domain in all known AMPK core structures have so far hampered a molecular explanation for AMP-dependent activation of the holo-complex. This mechanism necessarily involves a cross-talk between AMP binding on γ and the activating Thr¹⁷² phosphorylation on the α kinase domain, which most likely implies a conformational change and/or a domain movement. Therefore, detailed analysis of the full-length mammalian AMPK heterotrimer and its dynamic structure upon activation is obviously necessary.

Here we report on the molecular shape of γ_1 -containing AMPK holoenzyme complexes obtained using different biophysical approaches. We have set up a high level expression and automated purification protocol of untagged AMPK protein on the basis of our His₆-tagged tricistronic expression system (45). It yields sufficient quantities of homogeneous functional kinase complexes without the need of a potentially interfering purification tag. This allowed us to study AMPK in solution by small angle x-ray scattering (SAXS) and by different electron microscopy techniques, including single particle reconstruction. These data characterize AMPK as an elongated, flat particle with a large indentation and protrusions. Importantly, they demonstrate a ligand-induced conformational change of the AMPK heterotrimer upon binding of AMP.

EXPERIMENTAL PROCEDURES

Plasmids and Expression of Proteins in Bacteria—Tricistronic AMPK expression plasmids were constructed as described earlier (45), but encoding non-tagged versions of the four different mammalian AMPK isoform combinations $\alpha_1\beta_1\gamma_1$, $\alpha_2\beta_1\gamma_1$, $\alpha_1\beta_2\gamma_1$, and $\alpha_2\beta_2\gamma_1$ (GenBankTM accession numbers U40819, Z29486, X95577, AJ224538, and X95578). Proteins were expressed in Tuner (DE3) *Escherichia coli* cells (Novagen, EMD Chemicals Inc., Darmstadt, Germany). Expression of AMPK in rich medium in a self-constructed fermenter is described elsewhere (46). Preculturing and expression in minimal medium was developed for full-length heterotrimeric AMPK and was also later successfully applied for the expression of the LKB1 complex as described recently (47). The same method was used here for AMPK expression in a 42-liter bioreactor (MBR Switzerland), except that the growth temperature was kept at 34 °C, or in a 5-liter bioreactor (Minifors, Infors AG, Switzerland), except for some adaptations to the reduced vessel volume. After inoculation with cells from 400 ml of pre-culture, batch growth was continued for 12 h overnight at 32 °C with a stirrer speed at 1000 rpm and an air flow of about 4 liters/min until depletion of glucose and acetate ($pO_2 \sim 100\%$). The feed was balanced with O₂ consumption until reaching the pO_2 limitation at the maximal air flow (~ 7 – 8 liters/min; to obtain such high air flow, the original air inlet filter was changed to an AcroPac 300, Pall, Switzerland) and maximal stirrer speed (1250 rpm). Protein expression was

induced with 50 mg/liter isopropyl 1-thio- β -D-galactopyranoside at around $OD_{600\text{ nm}} = 25$ for 7.5 h at 34 °C.

Bacteria were harvested by centrifugation, washed in physiological NaCl solution, and immediately frozen in liquid nitrogen. The yield per fermentation, expressed as wet weight of bacterial pellet, was reproducibly 200–250 or 1200–1400 g in the 5- or 42-liter bioreactor with 3 or 27 liters of medium, respectively.

Protein Extraction—A 70-g aliquot of the frozen bacterial pellet was resuspended in lysis buffer (LysB: 30%(w/v) glycerol, 0.5 M sucrose, 50 mM HEPES, 2 mM $MgCl_2$, pH 8.0, at 7 °C) to a total volume of about 200 ml. Cells were lysed with an Emulsiflex C5 high pressure homogenizer (Avestin, Germany), first applying 100–300 bar to resuspend cells, and then using 1200–1500 bar for cell lysis. The lysate was supplemented with 7 μ l of Benzonase (purity grade II, Merck, Germany), stirred gently at 4 °C for 1 h, and centrifuged at $23,000 \times g$ for 1 h to pellet cell debris. The clear supernatant was used for HPLC purification.

Protein Purification—A new protocol was developed based on (i) the fact that untagged AMPK heterotrimer is able to bind to some metal affinity matrices, and on (ii) the availability of an Äkta Explorer 100 Air HPLC system (GE Healthcare) that was modified to allow automated multidimensional purification. Details of the machine setup will be published elsewhere.⁵ The setup used here included the following columns: (i) XK 26/40 (GE Healthcare) containing 140 ml of Protino Ni-IDA (Macherey Nagel, Switzerland), (ii) XK 26/20 containing 45 ml with Reactive Red 120 fast flow highly cross-linked 6% agarose (R-6143 Sigma), (iii) two 1-ml Ni-HP columns (GE Healthcare), (iv) Superdex 200 16/60 (GE Healthcare); as well as a 10-ml Super-loop (SL) (GE Healthcare) at the first injection valve. The buffers used were: elution buffer (EluB: as LysB, but with the addition of 250 mM imidazole), Red Sepharose elution buffer (RSEluB: as LysB, but with the addition of 600 mM NaCl), Ni-HP elution buffer (HPEluB: as EluB but with the addition of 200 mM NaCl and 2 mM Tris(2-carboxyethyl)phosphine hydrochloride), size exclusion buffer one (SE1: 200 mM NaCl, 50 mM HEPES, 10 mM $MgCl_2$, 8 mM EDTA, 2 mM Tris(2-carboxyethyl)phosphine hydrochloride, pH 8.0, at 7 °C), and size exclusion buffer two (SE2: as SE1, but without EDTA and with only 2 mM $MgCl_2$).

The fully automated purification procedure was carried out at 7 °C except for the Superdex column, which was run at 25 °C. Sample tubing at S1, S2, and S3 were connected to vessels containing LysB, EluB, and RSEluB, respectively, and were primed manually. The Ni-IDA column was equilibrated with LysB, the Reactive Red column with EluB, and the Ni-HP column with RSEluB. Tubing and valves were flushed with the appropriate buffers. Bacterial lysate was added to the sample vessel S1 and the automated run was started. Lysate was then applied to the Ni-IDA column at a flow rate of 4 ml/min using an air sensor to stop direct load injection. The column was washed with 160 ml of LysB (flow rate 5 ml/min at maximal 0.5 MPa pressure feedback). After flushing the system and P960 with EluB, bound proteins were eluted with EluB (5 ml/min, maximum 0.5 MPa).

Elution fractions between 63 and 156 ml after EluB application were recovered in the S2 vessel and re-injected into the Reactive Red column at a flow rate of 1 ml/min, maximum 0.2 MPa. After washing with 94 ml of LysB at 2 ml/min (maximum 0.2 MPa), the volume eluting between 20 and 95 ml after application of RSEluB was collected in the S3 vessel and re-injected into the Ni-HP columns (1 ml/min, maximum 0.4 MPa). Columns were washed with 8 ml of LysB (0.5 ml/min, maximum 0.4 MPa) and eluted with EluB. A 5-ml peak fraction (starting at $A_{280} > 0.6$) was collected in the SL. The Superdex column was equilibrated with 200 ml of SE1 buffer (1.6 ml/min, maximum 0.1 MPa) and, finally, 4 ml of the SL fraction were loaded and 1-ml fractions were collected. Material left in the tubing and SL was collected later in separate fractions.

For mass spectrometry (MS), STEM, transmission electron microscopy (TEM), SAXS, crystallization, and activity experiments, the first part of the size exclusion peak showing the highest specific AMPK activity was pooled, and subjected to a second size exclusion chromatography on the same Superdex column but using SE2 buffer without EDTA. Protein concentrations were determined using the Bradford Bio-Rad microassay (Bio-Rad) in SE2 buffer, calibrated by the 280-nm extinction coefficient for unfolded AMPK protein ($\alpha_1\beta_1\gamma_1$, 0.911; $\alpha_2\beta_2\gamma_1$, 0.892 g/liter).

Dynamic Light Scattering—The dynamic light scattering signal was recorded on a DynaPro molecular sizing instrument (Wyatt). Samples after elution from the second size exclusion chromatography were concentrated to 10 mg/ml in SE2 buffer and centrifuged at $20,000 \times g$ at 4 °C for 30 min prior to the measurements. Data were acquired using a 50- μ l sample in an Eppendorf UVette cuvette at 20 °C with 10-s acquisition intervals and maximum laser intensity and analyzed with the software Dynamics.

Enzyme Activity Assay—Following full activation by upstream kinases, activity of purified AMPK was determined by phosphorylation of the synthetic substrate SAMS in the presence of saturating AMP concentrations, using a non-radioactive, HPLC-based method that quantifies SAMS, phospho-SAMS, AMP, ADP, and ATP, as described previously (10).

Scanning Transmission Electron Microscopy (STEM)—Cross-linking of 1 mg/ml AMPK obtained in SE2 buffer after a second size exclusion chromatography was done at a final concentration of 1% glutaraldehyde (Fluka, Switzerland) for 60 s on ice and quenched with Tris, pH 8.0, at 4 °C. The cross-linked AMPK was then repurified by size exclusion on column 4 in SE2 to remove aggregates. An aliquot of this preparation was diluted 4 \times in SE2 buffer, and 5- μ l aliquots were adsorbed for 60 s to glow-discharged STEM films (thin carbon films that span a thick fenestrated carbon layer covering 200-mesh/inch, gold-plated copper grids). The grids were blotted, washed on 5 drops of quartz double-distilled water, freeze-dried at -80 °C and 5×10^{-8} torr overnight in the microscope. Tobacco mosaic virus particles (kindly provided by R. Diaz Avalos, University of California, Davis, CA) were used for absolute mass calibration. These particles were similarly adsorbed to separate STEM films, washed on 4 drops of 10 mM ammonium acetate, and air-dried. A Vacuum Generators STEM HB-5 interfaced to a modular computer system (Tietz Video and Image Processing

⁵ U. Riek, S. Ramirez, T. Wallimann, and U. Schlattner, unpublished data.

Structural Properties of AMPK

System GmbH, Gauting, Germany) was employed. Series of 512×512 -pixel, dark-field images were recorded from the unstained sample at an acceleration voltage of 80 kV and a nominal magnification of $\times 200,000$. The recording dose ranged from 474 to 945 electrons/nm². The digital images were evaluated using the software package IMPSYS (48). Accordingly, the projections were selected in circular boxes, and the total scattering of each region was calculated. The background scattering of the carbon support film was then subtracted, and the mass was calculated. The results were scaled according to the mass measured for tobacco mosaic virus and corrected for beam-induced mass loss according to the behavior of proteins in a similar mass range (49).⁵ The mass values were then displayed in histograms and described by Gaussian curves. The overall experimental uncertainty of the results was estimated from the corresponding S.E. (S.E. = S.D./ \sqrt{n}) and the approximate uncertainty of 5% in the calibration of the instrument. The number of particles giving rise to each peak, n , was estimated by measuring between the points of peak overlap.

To aid peak assignment, galleries were created displaying particles with masses ± 20 kDa from each peak. Average images were calculated using the EMAN program package (50).

TEM and Image Processing—AMPK samples were diluted (in SE2) to 20 $\mu\text{g/ml}$. Aliquots of 5 μl were stained with 2% (w/v) uranyl acetate after sample adsorption onto glow discharged 400-mesh carbon-coated grids. The micrographs were recorded at an accelerating voltage of 100 kV and a magnification of $\times 50,000$, using a Hitachi 7000 electron microscope. All micrographs were recorded on Kodak SO-163 film. The electron micrographs were digitized with a Heidelberg Primescan (Germany) scanner at 4 $\text{\AA}/\text{pixel}$ (resolution at the sample level). Manually selected particle projections were subjected to reference-free alignment and classification by multivariate statistical analysis using the EMAN software package (50). The class averages with the best signal-to-noise ratio were gathered in a gallery.

MS—The AMPK complex was analyzed after chemical cross-linking performed with a mixture of cross-linkers (CovalX K100 MALDI MS stabilization kit, Zurich, Switzerland). The cross-linking chemistry and specificity has been studied and described (51). 10 μl of AMPK complex at 2 μM was submitted to the cross-linking reactions and incubated on ice for 1 h to achieve complete reaction. After cross-linking, 1 μl of the sample containing the stabilized complex was mixed with 1 μl of the matrix solution of sinapic acid (10 mg/ml) in acetonitrile/deionized water 1:1 (v/v) and 0.1% trifluoroacetic acid. After mixing, 1 μl of the mixture was dropped onto the MALDI plate using the dried droplet method.

High mass MALDI-TOF mass spectra were obtained using a Reflex III MALDI-TOF mass spectrometer (Bruker Daltonics, Bremen, Germany) equipped with a HM1 high-mass detection system (CovalX, Zurich, Switzerland). The instrument was operated in linear mode by applying an accelerated voltage of 25 kV. Mass spectra were acquired by averaging 200 shots. The laser pulse energy was adjusted slightly above threshold for ion production. The mass spectra were acquired after external calibration with a mixture of 4 proteins covering a 6–150-kDa range. The mass spectrometric data were analyzed using Com-

plex Tracker software (CovalX AG). The software allows the overlay and subtraction of control and cross-linked spectrum for characterization of intact protein complexes analyzed by high mass MALDI-TOF mass spectrometry.

SAXS—The synchrotron SAXS data were collected at DESY (Hamburg, Germany) on the X33 camera of the EMBL (52, 53). Two isoforms of wild type AMPK ($\alpha_1\beta_1\gamma_1$ and $\alpha_2\beta_2\gamma_1$) in SE2 with and without 1 mM AMP were analyzed at protein concentrations ranging from 0.5 to 18 mg/ml. Data were recorded using a MAR345 image plate detector at a sample-detector distance of 2.4 m and a wavelength $\lambda = 0.15$ nm, covering the range of momentum transfer $0.12 < s < 4.5$ nm⁻¹. No radiation damage was observed during two 2-min test exposures. The data were reduced, processed, and the overall parameters computed following standard procedures of the software package PRIMUS (54, 55).

The forward scattering $I(0)$ and the radius of gyration R_g were evaluated using the Guinier approximation (56) assuming that at very small angles ($s < 1.3/R_g$) the intensity is represented by $I(s) = I(0) \exp(-1/3(sR_g)^2)$. These parameters were also computed from the entire scattering patterns using the program GNOM (57), also yielding the maximum particle dimension D_{max} . The molecular masses of the solutes were evaluated by comparing forward scattering with that of reference solutions with bovine serum albumin. The excluded volume of the hydrated particle (Porod volume V (58)) was computed using Equation 1,

$$V = 2\pi^2 I(0) / \int_0^\infty s^2 I_{\text{exp}}(s) ds \quad (\text{Eq. 1})$$

(I_{exp} experimental data as function of momentum transfers).

Prior to this analysis, an appropriate constant was subtracted from each data point to force the s^{-4} decay of the intensity at higher angles following Porod law for homogeneous particles. This “shape scattering” curve was further employed to generate low resolution *ab initio* models of monomeric AMPK heterotrimers using the program DAMMIN (59), which represents the protein by an assembly of densely packed beads. Simulated annealing is employed to build a compact interconnected configuration of beads inside a sphere with the diameter D_{max} that fits the experimental data $I_{\text{exp}}(s)$ to minimize discrepancy,

$$\chi^2 = \frac{1}{n-1} \sum_j \left[\frac{I_{\text{exp}}(s_j) - c I_{\text{calc}}(s_j)}{\sigma(s_j)} \right]^2 \quad (\text{Eq. 2})$$

where n is the number of experimental points, c is a scaling factor, and $I_{\text{calc}}(s_j)$ and $\sigma(s_j)$ are the calculated intensity and the experimental error at the momentum transfer s_j , respectively. The results from 10 runs for each type were averaged using the program DAMAVER (60), which superimposed the models pairwise to generate the most typical model by retaining the common structural features.

RESULTS

Purification—The presence of a purification tag in a recombinant protein may cause problems for its biophysical or bio-

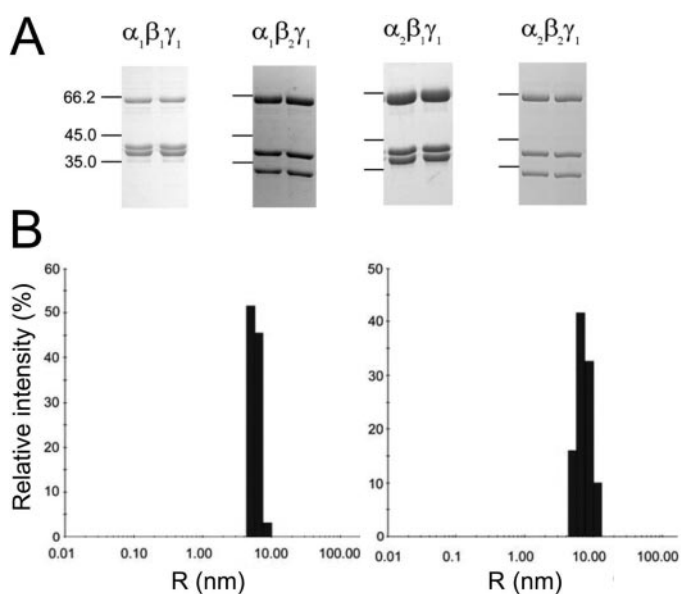


FIGURE 1. **SDS-PAGE and DLS of AMPK.** A, Coomassie Blue-stained SDS-PAGE (12%), showing the purity of the full-length, untagged AMPK heterotrimeric isoforms purified with the four-dimensional method described herein. Note: the β_2 chain shows anomalous electrophoretic migration behavior. B, dynamic light scattering of two typical samples of concentrated $\alpha_2\beta_2\gamma_1$ -AMPK (10 mg/ml) in SE2 buffer, showing a polydispersity of $\sim 20\%$.

chemical characterization, especially for crystallization. Attempts to remove the His tag from tagged AMPK after purification were unsuccessful, partly due to precipitation of AMPK after cleavage and protein loss during IMAC employed to remove uncleaved AMPK. Further analysis revealed that untagged AMPK also bound to the IMAC column (data not shown). Based on this finding, a four-dimensional purification protocol was developed on a highly modified commercial HPLC.⁵ It applies first IMAC, second a nucleotide analog affinity chromatography (Reactive Red 120-agarose), third another IMAC for sample concentration, and fourth a preparative size exclusion column. This procedure was automated and optimized for minimum total run time (~ 18.5 h, supplemental Fig. 2A), convenience, and reproducibility, rather than maximum yield (about 10–15 mg of AMPK per 70 g wet weight bacterial pellet). Several subunit isoform combinations ($\alpha_1\beta_1\gamma_1$, $\alpha_2\beta_1\gamma_1$, $\alpha_1\beta_2\gamma_1$, and $\alpha_2\beta_2\gamma_1$) were bacterially expressed and purified according to this protocol. AMPK eluted from the final calibrated gel filtration column at an elution volume corresponding to ~ 240 kDa. This is a higher molecular mass than expected for heterotrimers, indicating a strong non-sphericity of these particles. Coomassie Blue-stained SDS-PAGE gels of the peak fractions revealed the general homogeneity of the preparations with three distinct protein bands at the expected molecular weight corresponding to the α -, β -, and γ -subunits of AMPK (Fig. 1A).

A final, second size exclusion chromatography run was performed to remove EDTA, which was included in the buffer of the first size exclusion chromatography to chelate Ni^{2+} ions leaking from the preceding IMAC column. Functional integrity of these final AMPK preparations was verified by activity determination using CaMKK β for activation and AMP for maximal stimulation. Maximal specific activities of the elution fractions

were further increased compared with the first size exclusion step, ranging from ~ 4 to ~ 6 μmol of phospho-SAMS min^{-1} mg^{-1} (supplemental Fig. 2B), which is comparable with those reported earlier (10). However, it should be noted that specific kinase activity was always slightly higher in the first half of the size exclusion peak.

Taken together, the new automated protein purification scheme resulted in highly purified and enzymatically functional untagged full-length AMPK. Either such untagged protein or the earlier His₆-tagged version (45) have been successfully used in several studies (10, 19, 61–68).

Dynamic Light Scattering— $\alpha_1\beta_1\gamma_1$ - and $\alpha_2\beta_2\gamma_1$ -AMPK samples concentrated to 10 mg/ml showed a polydispersity of about 20% and a hydrodynamic radius of about 5.6–7.5 nm in dynamic light scattering (Fig. 1B). This results in a calculated molecular mass range of 210–380 kDa. Because the expected molecular mass of the $\alpha\beta\gamma$ AMPK heterotrimers is roughly 130 kDa, this data suggests the formation of dimers or higher oligomers at elevated protein concentration.

Scanning Transmission Electron Microscopy—For mass determination by STEM, a solution of $\alpha_2\beta_2\gamma_1$ -AMPK at 1 mg/ml was reacted with 1% glutaraldehyde to conserve the native complexes prior to the dilutions required for microscopy. The cross-linking efficiency was verified by SDS-PAGE and any large unspecific oligomers were removed by size exclusion chromatography as described above. The unstained AMPK particles were imaged by STEM (Fig. 2A), manually sorted according to their dimensions (small, medium, and large), and subsequently analyzed for their mass as shown in the three histograms (Fig. 2, B–D). The major particle population (Fig. 2, B and C) mainly contained single heterotrimers (expected molecular mass ~ 130 kDa) including the peaks at $142 (\pm 33)$ kDa ($n \sim 766$; arrow in Fig. 2B) and $130 (\pm 21)$ kDa ($n \sim 124$; arrow in Fig. 2C). These two peaks arise from particles of different size ($\sim 11 \times 8$ and $\sim 8 \times 7$ nm in diameter; estimated uncertainty in longest dimension ± 1 nm), which may be interpreted as side and top views of the heterotrimer. A minor particle population (Fig. 2D) showed a peak at $296 (\pm 28)$ kDa ($n \sim 73$; arrow in Fig. 2D), indicating the additional presence of dimers of AMPK heterotrimers as already seen by dynamic light scattering experiments in more concentrated solutions. The minor histogram peak at $83 (\pm 21)$ kDa ($n \sim 36$; Fig. 2C) is not significant and may be assigned to a small number of disassociation products, whereas the peaks at 221 and $392 (\pm 28)$ kDa ($n \sim 52$ and ~ 17 , respectively; Fig. 2D) relate to some unspecific association. The existence of AMPK heterotrimers and dimers thereof was corroborated by prior SDS-PAGE separations of cross-linked AMPK material (not shown).

High Mass MALDI-TOF MS—To analyze the composition of AMPK complexes, the $\alpha_2\beta_2\gamma_1$ -AMPK was subjected to high mass MALDI-TOF MS. Without chemical cross-linking, three different polypeptides were detected in the overlay spectrum (Fig. 3A, black trace: $m/z = 62.26$, 30.24 , and 37.38 kDa). They very precisely correspond to the expected molecular mass of the three individual subunits α_2 (62.32 kDa), β_2 (30.23 kDa), and γ_1 (37.58 kDa). To distinguish between $\alpha_2\beta_2\gamma_1$ heterotrimers (130.13 kDa) and a possible $(\beta_2\gamma_1)_2$ complex of similar size (135.56 kDa), MS of the entire cross-

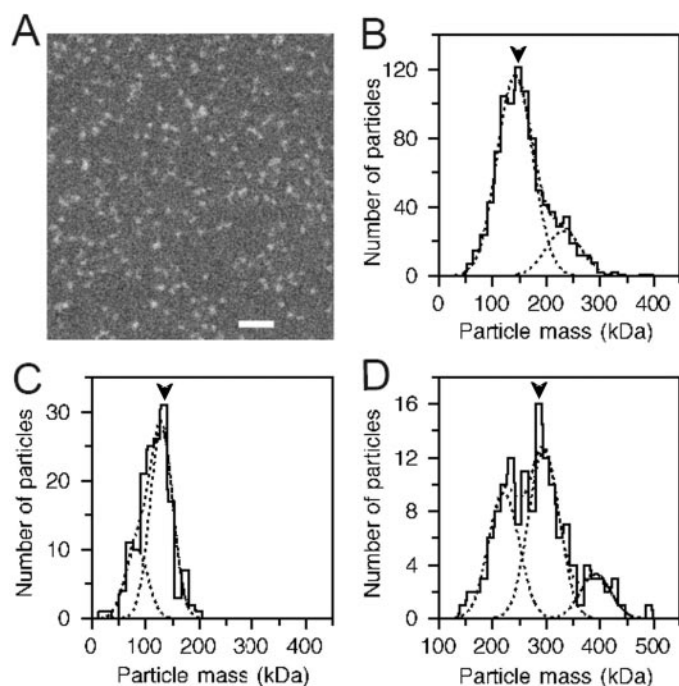


FIGURE 2. STEM picture and mass determination of glutaraldehyde cross-linked $\alpha_2\beta_2\gamma_1$ -AMPK. *A*, section of a STEM picture used for mass determination, scale bar = 50 nm. *B*, histogram for the main medium size population of AMPK: 142 and 232 (± 33)⁺ kDa ($n^* \sim 766$ and 154, respectively); the 142-kDa species corresponds to monomeric AMPK heterotrimers. *C*, histogram for the smallest particles: 83, 130 (± 21)⁺ kDa ($n^* \sim 36,124$, respectively), corresponding to partially dissociated AMPK complex species (83 kDa) or heterotrimers (130 kDa). *D*, histogram for the largest particles: 221, 296, and 392 (± 28)⁺ kDa ($n^* \sim 52, 73$, and 17, respectively), with the 296-kDa species corresponding to the dimer of heterotrimers). *, the values of n are approximate and are measured between the points of peak overlap. +, the standard deviations are within the size expected from background fluctuations.

linked AMPK complexes was conducted (Fig. 3A, red trace). Intact complex was clearly detected with $m/z = 129.95$ kDa, corresponding to the $\alpha_2\beta_2\gamma_1$ heterotrimer. The subtraction spectrum (Fig. 3B) confirmed the presence of the heterotrimer ion $[\alpha_2\beta_2\gamma_1]^{1+}$, together with a peak at $m/z = 64.97$ kDa representing the doubly charged heterotrimer $[\alpha_2\beta_2\gamma_1]^{2+}$. These data corroborate the correct heterotrimeric stoichiometry and the absence of $(\beta\gamma)_2$ complexes.

Transmission Electron Microscopy—TEM of negatively stained $\alpha_2\beta_2\gamma_1$ -AMPK revealed a major population of elongated particles with a maximum length of ~ 11 nm (± 1 nm, Fig. 4). Comparison with the dimensions of the ~ 130 – 140 -kDa particles analyzed by STEM, allowed their assignment as heterotrimers. Reference-free alignment and classification of 937 such particles yielded class averages corresponding to different orientations of the molecules on the carbon film. The molecules appear elongated and show some cavities giving them a “cashew nut”-like appearance.

Small Angle X-ray Scattering—Particle characterization in solution with SAXS was applied to wild type AMPK of the two-subunit isoform combinations $\alpha_1\beta_1\gamma_1$, and $\alpha_2\beta_2\gamma_1$. The experimental SAXS curves for different protein concentrations are shown in Figs. 5 and 6, the corresponding integral structural data are presented in Table 1.

First of all, the data show that the size of the scattering particle depends on the protein concentration. At high AMPK

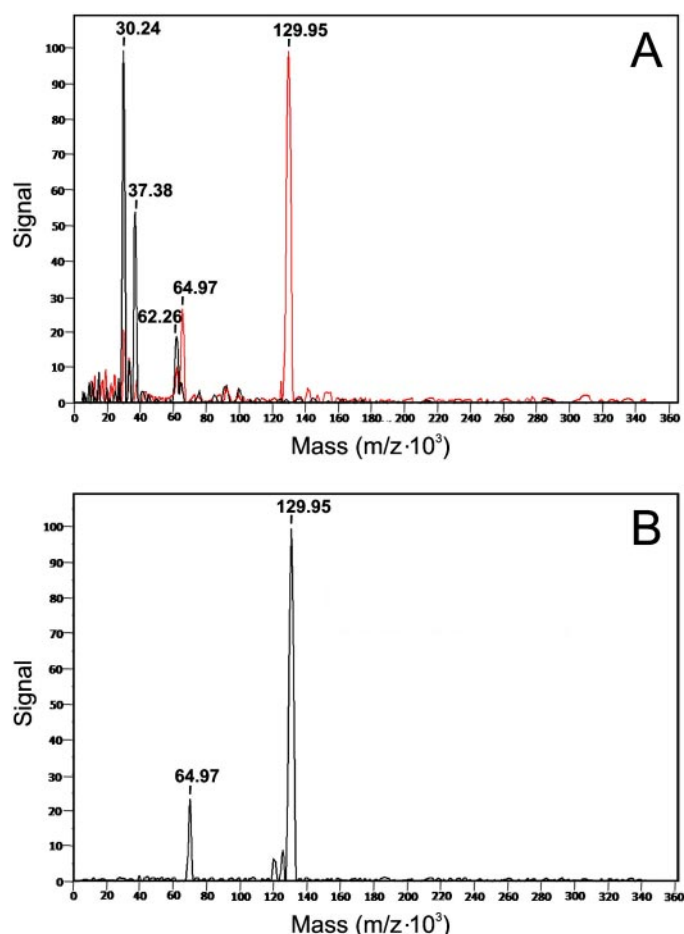


FIGURE 3. High mass MALDI spectra of the heterotrimeric $\alpha_2\beta_2\gamma_1$ -AMPK complex and single subunits. *A*, overlay spectra of AMPK complex analyzed before cross-linking (black trace) clearly showing the mass of the single subunits (30.24 kDa for β_2 , 37.38 kDa for γ_1 and 62.26 kDa for α_2) and after cross-linking (red trace) showing intact $\alpha_2\beta_2\gamma_1$ complex (129.95 kDa). *B*, subtraction spectrum obtained by subtracting the control spectrum from the cross-linked spectrum. It reveals the predominance of the heterotrimer complex $[\alpha_2\beta_2\gamma_1]$ with $m/z = 129.95$. Note that the peak at 64.97 kDa corresponds to the doubly charged heterotrimer ion $[\alpha_2\beta_2\gamma_1]^{2+}$.

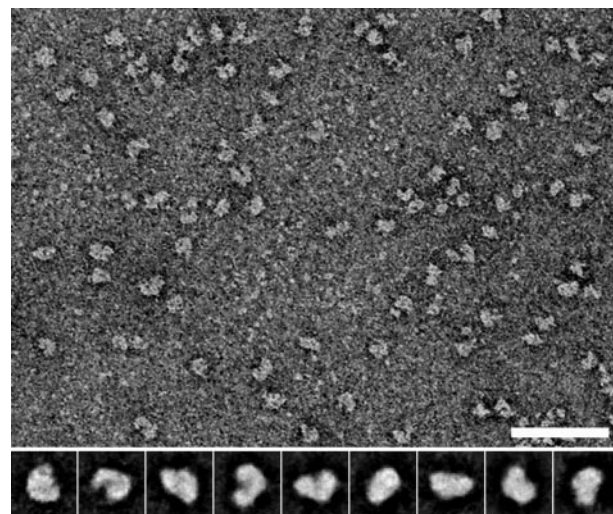


FIGURE 4. Electron microscopy of negatively stained $\alpha_2\beta_2\gamma_1$ AMPK. The scale bar corresponds to 50 nm. The insets display the averaged images of the major classes of a total of 937 handpicked images, representing different orientations of the particle on the carbon support. The inset baselines each correspond to 18 nm.

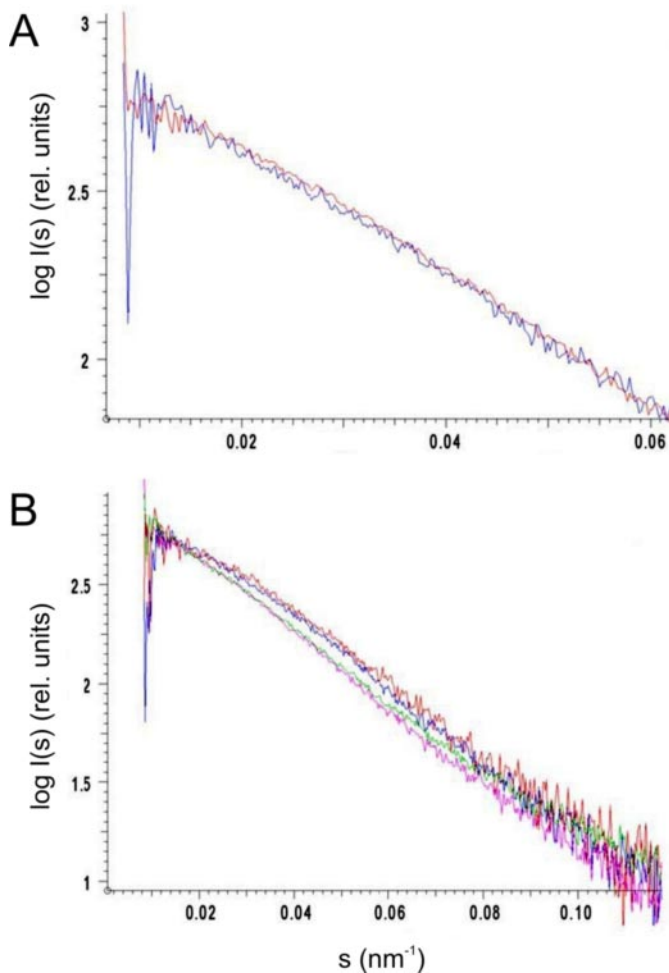


FIGURE 5. Small angle x-ray scattering curves of AMPK in solution. The \log_{10} of the radially symmetric scattered x-ray intensity around $I(0)$ is plotted as a function of the momentum transfer s . The large congruence of the scattering curves from $\alpha_1\beta_1\gamma_1$ -AMPK in the diluted solution of 1.00 (blue) and 0.50 mg/ml (red), after scaling to the protein concentration, indicates that no further decrease of maximum size and radius of gyration of AMPK particles occurs within this protein concentration range. *B*, diluted, monodisperse AMPK solutions of $\alpha_1\beta_1\gamma_1$ (without AMP magenta; with AMP, green) and $\alpha_2\beta_2\gamma_1$ (without AMP, blue; with AMP, red), showing a small but significant change upon AMP ligand binding.

concentrations generally used for SAXS, an oligomerization of AMPK occurred (Fig. 6 and Table 1). AMPK concentrated to 10–20 mg/ml occasionally showed some unspecific large aggregates, but mostly specific, larger but homogeneous particles ($D_{\max} \sim 25$ –30 nm) in the size range of AMPK heterotrimer dimers. Upon dilution of such concentrated AMPK solutions, a decrease of R_g and D_{\max} was observed, leading to values similar to those observed for samples that had always remained at low protein concentration. Therefore, the observed dimerization of AMPK heterotrimers is a reversible, concentration-dependent process. Upon decreasing the AMPK concentration further to below ~ 1 mg/ml (Fig. 5A and Table 1), the scattering signal became concentration-independent and no further decrease of maximum size and radius of gyration of AMPK particles occurred for both, $\alpha_1\beta_1\gamma_1$ - and $\alpha_2\beta_2\gamma_1$ -AMPK. Such ideal, monodisperse solutions (in SAXS terms) were represented by a homogeneous population of monomers of AMPK heterotrimers with a maximum particle dimension D_{\max} of 16 ± 1 nm, a

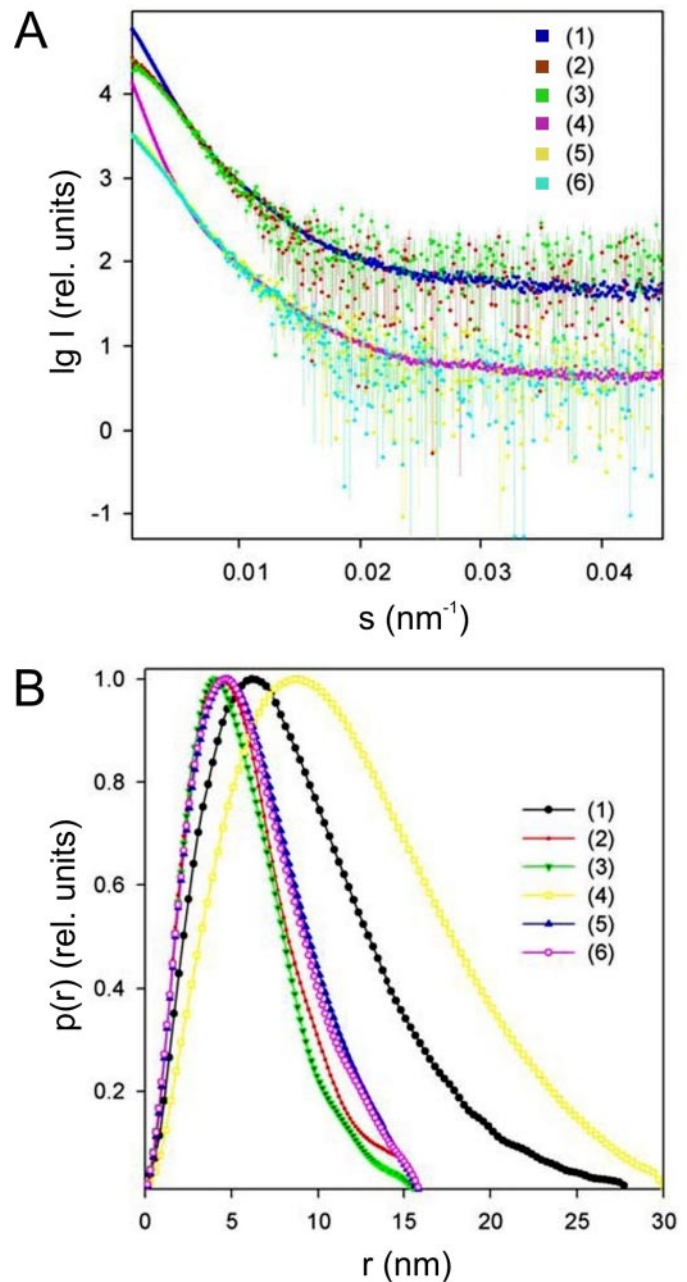


FIGURE 6. SAXS curves of AMPK isoforms and corresponding distance distribution functions. Scattering curves in *A* and distance distribution functions in *B* at different concentrations show the effect of concentration-dependent reversible dimerization of AMPK heterotrimers. Scattering curves 4–6 are scaled by a factor 10 for graphical comparison. 1–3, $\alpha_2\beta_2\gamma_1$ -AMPK: 1, high concentration (13 mg/ml); 2, low concentration (0.4 mg/ml); 3, low concentration (0.4 mg/ml) + AMP. 4–6, $\alpha_1\beta_1\gamma_1$ -AMPK: 4, high concentration (17.6 mg/ml); 5, low concentration (0.8 mg/ml); 6, medium concentration (2.2 mg/ml) + AMP.

maximum distance distribution function of ~ 5 nm, and a molecular mass of roughly 140 kDa. The larger dimensions and additional mass of heterotrimers compared with calculated data and to those determined in TEM/STEM can be explained by the presence of the hydration shell and the potential flexibility of the AMPK complex (69), both of which increase the size seen by SAXS. Furthermore, in the case of EM, an influence of adsorption on the flexible AMPK heterotrimer cannot be

Structural Properties of AMPK

entirely ruled out, and interaction with the carbon film of the grid might favor more compact conformations of the complex.

The latter ideal AMPK solution, *i.e.* a protein concentration below ~ 1 mg/ml, is a precondition to study the binding of the ligand AMP, or to model the heterotrimeric AMPK particle from SAXS data. Addition of the allosteric activator AMP induced a noticeable change in the AMPK scattering curves (Fig. 5B) and in the derived radii of gyration (R_g , Table 1), whereas the maximum particle dimension (D_{\max} , Table 1) remained constant. This clearly indicates that AMP binding leads to more compact particles (Fig. 6A). At higher, non-monodisperse protein concentrations, addition of AMP also decreased R_g (not shown). However, these results are ambiguous, because it is impossible to distinguish between effects caused by changes in the dimerization equilibrium induced upon ligand binding and changes in the shape of the scattering particles themselves.

Models of the molecular shape of monodisperse heterotrimeric $\alpha_1\beta_1\gamma_1$ - and $\alpha_2\beta_2\gamma_1$ -AMPK in solution were calculated using the DAMMIN software in the “keep” mode and assuming P1 symmetry (no symmetry). Individual molecules were represented by elongated, curved particles showing a deep indentation and protrusions (Fig. 7). Some of these features are less evident in averaged and filtered models based on 10 different, individual models each calculated from data obtained without (Fig. 8, *green*) or with AMP added (Fig. 8, *red*). Arithmetic averages of the radii of gyration and the excluded model volumes calculated from these models by DAMMIN again showed a consistent and significant change of about 5% toward a more compact scattering particle upon AMP ligand binding.

DISCUSSION

This study provides a first detailed structural characterization of untagged, full-length and enzymatically competent het-

erotrimeric AMPK by applying a variety of independent but complementary biochemical and biophysical analytical tools. The quantitative results obtained suggest that AMPK heterotrimers are not spherical but rather elongated, curved particles that have a strong tendency to dimerize. Most importantly, allosteric activation by AMP is shown to involve a conformational change toward a more compact heterotrimer.

Large Quantities of Untagged, Native AMPK Are Essential for Biophysical Analysis—High yield bacterial expression and the novel purification protocol for untagged AMPK were instrumental for this study, providing the large amounts of purified, native protein required for biophysical characterization, especially for SAXS or isothermal titration calorimetry (ITC). Implementation of the automated four-dimensional purification procedure was aimed at increased reproducibility and minimal process time without reducing the purity of the final preparation. This was achieved by the use of frozen bacterial pellet aliquots from single fermentation runs and the setup of a user-modified Äkta ExplorerTM.⁵ The latter provided reproducible instrumental precision, reduced the time needed for purification to about 18.5 h overnight (as compared with 1 week with manual operation), and gave a final overall yield of about 10–15 mg of AMPK per 70 g wet weight of bacterial pellet. Availability of freshly purified AMPK was in particular essential for methods that require large amounts of material and/or that are incompatible with glycerol, like SAXS, STEM, TEM, or ITC. Otherwise, addition of 50% glycerol is necessary to stabilize AMPK for longer time periods (10). Such purified AMPK could be activated by CaMKK β and further stimulated by the allosteric activator AMP, reaching a rather high specific activity of up to 6 μmol of phospho-SAMS $\text{min}^{-1} \text{mg}^{-1}$. In a previous study using this protein (10), we could show that AMP does not affect AMPK phosphorylation by the upstream kinases LKB1/MO25 α /STRAD α or CaMKK β (6–9), but inhibits AMPK dephosphorylation by protein phosphatases-2C α isoform (10). It was also shown that the combined activation effects are more than 1000-fold, thus much larger than thought previously (10). These data corroborate the functional integrity of the native AMPK preparations with respect to activation and deactivation mechanisms. To distinguish between the $\alpha\beta\gamma$ heterotrimers and possible ($\beta\gamma$) dimers with very similar molecular mass, MS of the entire cross-linked AMPK complexes was conducted. The data revealed a correct heterotrimeric stoichiometry and the absence of ($\beta\gamma$)₂ contamination.

Reversible Dimerization of AMPK at Higher Protein Concentrations—High concentrations of protein (above 10 mg/ml) are generally used for in solution characterization of

TABLE 1

Molecular properties of AMPK as determined by SAXS for two different AMPK isoform combinations at different concentrations

The abbreviations used are D_{\max} , maximal intramolecular distance; R_g , radius of gyration; MM, molecular mass; and V_{Porod} , particle volume according to Porod (58).

Samples	<i>c</i> mg/ml	D_{\max} nm	R_g nm	MM kDa	V_{Porod} nm^3
$\alpha_2\beta_2\gamma_1$	0.52	16.0	4.64	140	230
$\alpha_2\beta_2\gamma_1$	1.92	16.0	4.84	141	254
$\alpha_2\beta_2\gamma_1$	13.18	28.0	7.62	215	445
$\alpha_2\beta_2\gamma_1$ with AMP	0.51	16.0	4.44	137	211
$\alpha_1\beta_1\gamma_1$	0.50	16.0	5.13	133	310
$\alpha_1\beta_1\gamma_1$	1.00	17.0	5.14	139	315
$\alpha_1\beta_1\gamma_1$	17.62	30.0	9.26	330	590
$\alpha_1\beta_1\gamma_1$ with AMP	0.98	16.0	4.92	136	288

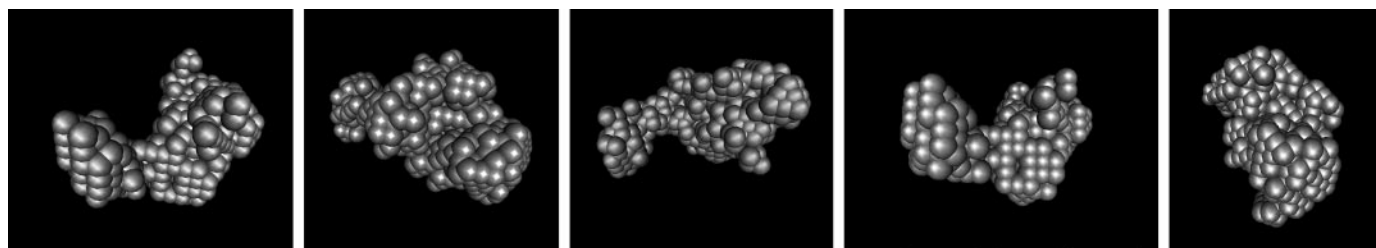


FIGURE 7. Gallery of selected views from an individual $\alpha_1\beta_1\gamma_1$ -AMPK model without AMPK ligand. The model demonstrates the similarity to the single particle TEM averages of AMPK. The diameter of the spheres is 8.5 Å.

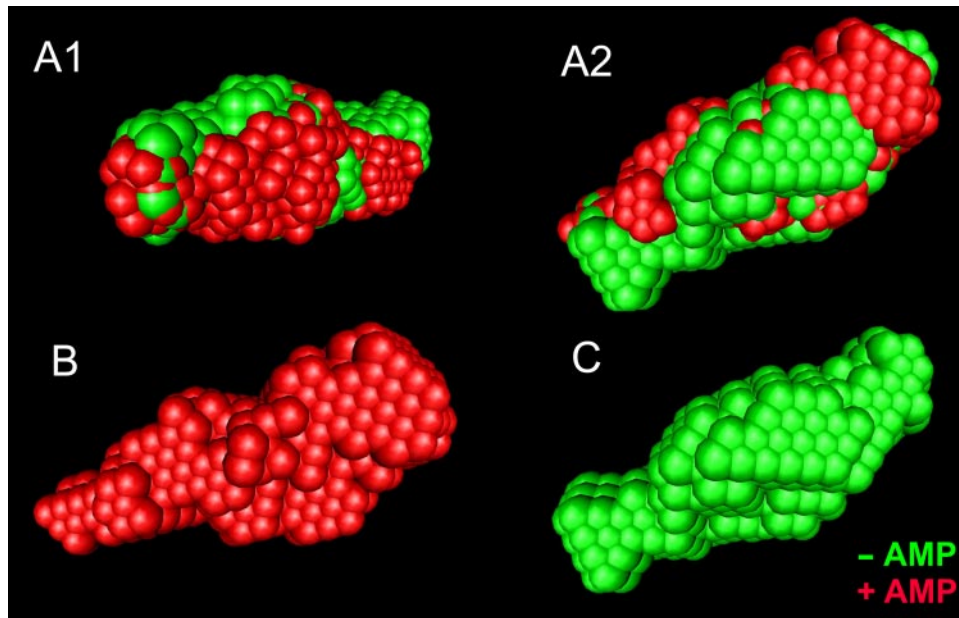


FIGURE 8. Gallery of averaged, filtered DAMMIN models of $\alpha_2\beta_2\gamma_1$ -AMPK. Each model was obtained by DAMAVER software, based on 10 individual models of each \pm AMP. Green, $\alpha_2\beta_2\gamma_1$ -AMPK without AMP, the cut-off volume is $2.440 \times 10^5 \text{ \AA}^3$. Red, $\alpha_2\beta_2\gamma_1$ apo-AMPK with AMP, the cut-off volume is $2.209 \times 10^5 \text{ \AA}^3$. Note, the diameter of the spheres building the space models is 8.5 Å for green and 7.4 Å for the red model. A1 and A2, two different views of the averaged models of $\alpha_2\beta_2\gamma_1$ -AMPK \pm AMP shown superimposed, centered on the center of mass and oriented along their axis of inertia. B, view of $\alpha_2\beta_2\gamma_1$ -AMPK with AMP approximately in the same orientation as in A2. C, view of $\alpha_2\beta_2\gamma_1$ apo-AMPK without AMP approximately in the orientation as in A2.

protein structures by SAXS to obtain an optimal signal to noise ratio. Under these conditions, the data revealed a strong tendency of AMPK heterotrimers to form dimers. In addition, the first results with SAXS and dynamic light scattering (not shown) indicated a concentration-dependent occurrence of further higher oligomers of the heterotrimer, as well as some unspecific aggregates or precipitates, especially upon exposition of the protein to stronger shearing forces by inappropriate handling, e.g. careless pipetting. This indicates a tendency of AMPK to form higher aggregates or to even denature *in vitro*, as also noted during the development of the AMPK purification protocol. However, if handled with sufficient care, AMPK did not just aggregate, but rather formed well defined dimers of native heterotrimers. This was confirmed independently by electron microscopy methods on a single molecule level. Dimers of AMPK heterotrimers were detected in small amounts by TEM, and also by STEM, the latter allowing exact mass measurements of oligomers after the chemical cross-linking.

As shown in further SAXS experiments, the dimerization process is a concentration-dependent and reversible process. Dilution of concentrated AMPK solutions led to a decrease in particle size, until values were reached comparable with those from AMPK samples that had been purified and maintained at such low protein concentrations. Samples diluted immediately (~ 1 min) before starting the 2-min x-ray exposure for SAXS were no different than undiluted low concentration samples or samples examined at a longer time after dilution. Therefore, the time scale for the reversible concentration-dependent dimerization equilibrium must be much less than 3 min.

Dimerization may in fact be an intrinsic, conserved property of the AMPK kinase family and even physiologically relevant.

The catalytic domain of SNF1, the yeast ortholog of AMPK, not only forms crystallographic dimers by a conserved and accessible surface motif, but also dimerizes in solution (38, 39, 70). Mammalian AMPK is not an abundant cellular protein, but different mechanisms may lead to higher local AMPK concentrations than commonly anticipated. These include compartmentation at defined subcellular loci (24, 71), e.g. in the cell nucleus or at biological membranes via the myristoyl anchor, and molecular crowding effects. Thus, it may be entirely reasonable to speculate that dimerization of AMPK could occur at such defined subcellular loci. However, for dimerization of AMPK to occur *in vivo*, not only is AMPK concentration important, but also the concentration of water in the cytosol and its activity coefficient(s) have to be considered.

AMP Binding to AMPK Induces a Conformational Change—Dilution of AMPK samples below 1 mg/ml did not result in a further decrease of particle size in SAXS, indicating that a thermodynamically ideal, monodisperse protein solution had been reached. This is an absolute prerequisite for the interpretation of SAXS data when analyzing ligand effects or for single particle modeling (see below). In such monodisperse AMPK solutions, binding of the allosteric activator AMP induced a clear and significant change in the particle conformation as directly seen by SAXS. The radii of gyration of both AMPK isoforms examined were reduced by about 5%, whereas the maximum particle dimensions remained constant. Comparative averaged SAXS models of AMPK with and without AMP (Fig. 8) indicate that the conformational change induced by ligand binding is likely to be a more radial movement of molecular mass, involving a domain movement tangentially along the long axis of the molecule, rather than an axially oriented shift of molecular mass. Such a change, together with the observed decrease of molecular mass by extrapolation to $I(0)$, as well as the decrease of both the Porod volume and the excluded DAMMIN model volume, would be consistent with a cleft-closing model in the AMPK heterotrimer upon binding of AMP due to loss of hydration shell water.

ITC was applied in an attempt to directly measure AMP binding constants to AMPK. Modern, state of the art microcalorimeters require AMPK concentrations significantly above 1.5 mg/ml to generate a signal that would allow analysis of the potentially three independent accessible AMP binding sites (two exchangeable sites in the Bateman domains, one in the kinase domain). However, as shown by SAXS, in this concentration range the dynamic, concentration-dependent dimerization equilibrium of AMPK heterotrimers is probably influenced by AMP binding, adding a further energy parameter to the sys-

tem and, thus, making ITC intrinsically unsuitable for the determination of the exact ligand binding constants for AMPK. So far, K_D values for AMP have been only determined for the Bateman domains in the isolated γ -subunits or the truncated mammalian core complex, ranging from 20 to 125 μM (12, 14). Thus, with the AMP concentration of 1 mM used in our study, we clearly saturated the AMP binding sites.

AMPK Heterotrimers Are Elongated, Curved Particles—In solution SAXS and single particle TEM were applied as complementary techniques to analyze molecular dimensions and shape of AMPK complexes. When using SAXS and procedures for particle reconstruction like DAMMIN, any deviation of an ideal solution has to be strictly avoided. Although heterotrimeric full-length AMPK can exist as monomers and dimers, the equilibrium between both is concentration-dependent. A monodisperse solution (in SAXS terms) of monomers of trimers was obtained at protein concentrations below 1 mg/ml (Table 1). However, this reduced the signal-to-noise ratio of SAXS measurements, especially at higher momentum transfer.

The STEM analysis provided a first estimate of both the mass and particle dimensions of the heterotrimers. This guideline ensured that the projections later selected from the negative stain TEM images and averaged (Fig. 5) indeed arose from heterotrimers.

Some differences in particle dimensions between SAXS and single particle TEM were observed. The maximum distance D_{max} inside the scattering AMPK particle, obtained by the distance distribution functions in SAXS, was 16 ± 1 nm, whereas particles with a size of 11 ± 1 nm were obtained by TEM with negatively stained AMPK and by STEM with cross-linked AMPK, respectively. Such differences may be largely due to the hydration shell and the rapid molecular dynamics of flexible AMPK molecules observed with the SAXS in-solution method (69). In addition, it cannot be excluded that more compact conformations were favored on adsorption to the EM grid adding to the size discrepancy.

Despite these explainable differences, the molecular shape of the SAXS models calculated by DAMMIN and the averaged pictures obtained by single particle TEM look strikingly similar. Both reveal large particles with an elongated, curved structure and a wider and a narrower end. This overall shape and appearance resembles that of a cashew nut. The SAXS models show an additional protrusion emanating perpendicularly from the more planar particle, as well as a deeper indentation. The latter feature is not seen so prominently in the TEM pictures, possibly due to a preferred orientation of the particles on the carbon film of the EM grid. Interestingly, the recent x-ray structure of the AMPK core complex of the *S. cerevisiae* AMPK homologue, SNF1, which contained most of the β -subunit, showed that the latter protruded perpendicularly to the long axis of the molecule (44). Thus, the protrusion resolved here by SAXS might either represent the kinase domain of the α -subunit or the β -subunit. However, the large truncations in the published high resolution x-ray structures (43, 44) preclude precise fitting of these data into the low resolution SAXS model.

The presence or absence of AMP also changed the appearance of the DAMMIN models of AMPK. Without AMP, the complex appeared very elongated with some protrusions

exposed, whereas AMP binding changed the molecule to a more compact shape preferentially at one end of the particle (compare Fig. 8, *A* and *B*). Because the heterotrimeric core of AMPK does not change conformation upon binding of AMP (14), the conformational change observed here by SAXS must have its structural basis in other parts of the molecule, *i.e.* in the α -subunit, which contains the kinase domain, or in the β -subunit, which contains the glycogen-binding domain. The conformational change upon AMP binding would thus be consistent with a relative movement of the α - and/or β -subunit, or domains thereof, along the long axis of the molecule toward the γ -subunit. This would lead to a change in mass distribution and thus to a more compact molecule. The fact that the regulatory domain of the α -subunit was shown to interact tightly with the γ -subunit in the *S. cerevisiae* SNF1 structure (44) would favor such an interpretation.

Full-length AMPK Reveals Properties Different to AMPK Core Complexes—The most recent x-ray structures of severely truncated core complexes of mammalian AMPK (14) and its orthologs in *S. pombe* (43) and *S. cerevisiae* (44) reveal two structural properties that are relevant to our study: (i) the yeast enzymes occur as crystallographic dimers of trimers, and (ii) no major conformational differences are observed between the apoenzyme and the AMP (or ATP)-bound states.

Tight dimers of yeast AMPK orthologs seem to occur readily in crystals (39, 43, 44), but also in solution (39). However, dimerization occurs at various different interfaces: between α - and γ -subunits in the *S. pombe* core complex (43) (whether this interface is accessible in the full-length holoenzyme remains an open question), between γ -subunits in the *S. cerevisiae* core complex (44), and between the kinase domains with individual Snf1 α -subunit orthologs (39). These latter interactions could also occur in the full-length heterotrimeric AMPK complex, but the mechanism of dimer formation in solution and its putative role *in vivo* await future clarification.

No significant conformational changes upon binding of AMP or ATP were observed in the *S. pombe* complex (43), or in the truncated mammalian AMPK (14). This may simply be due to the large truncations (Fig. 9), in particular to the absence of both the autoinhibitory and kinase domains (43). However, it is also unknown whether the yeast complexes are activated by AMP at all, thus precluding definite conclusions on the activation mechanism of mammalian AMPK. AMP binding to Bateman domains in the γ -subunit of mammalian AMPK leads to activation of the kinase domain in α , suggesting a cross-talk between these two subunits. The conformational change observed with full-length, native AMPK in our study provides a possible mechanism for this cross-talk.

A Model for AMPK Activation—Combining x-ray structural information (14, 43, 44) with known biochemical and biophysical data on the regulation of AMPK (10, 11) and the observed conformational change upon AMP binding (this work), we propose a new structural model for AMPK. The model is based on the AMPK ortholog of *S. cerevisiae* (Fig. 9A, PDB 2QLV, Ref. 44). Because only one AMP moiety was partially resolved (as in the *S. pombe* structure), the three AMP molecules observed in the mammalian AMPK core complex (14) were fitted into the homologous yeast sites by superposition. Turning the repre-

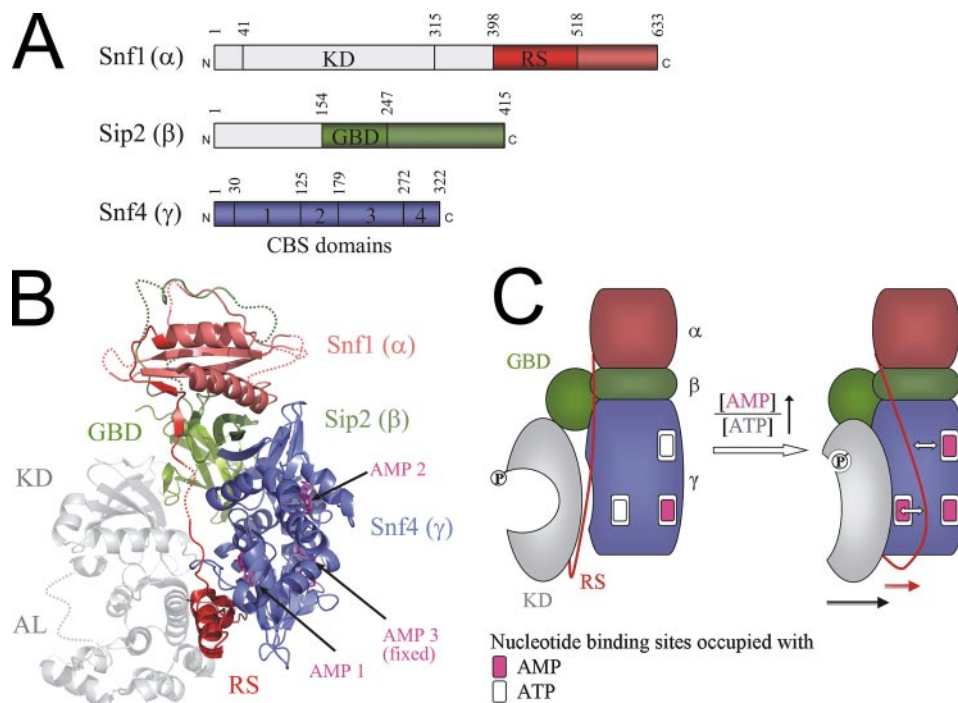


FIGURE 9. Model for AMPK activation by AMP: a novel role for the regulatory sequence. The model is mainly based on the recent x-ray structure of the *S. cerevisiae* AMPK ortholog core complex (44). Crystallized parts of the sequence are shown in: *red*, C terminus plus regulatory sequence (RS) of the α -subunit; *green*, C terminus plus glycogen-binding domain (GBD) of the β -subunit; *blue*, complete γ -subunit with the AMP-binding CBS domains. Bound AMP and ATP are in *magenta* or *white*, respectively. Sequence sections lacking corresponding structural information are in *gray*: e.g. kinase domain (KD) with activation loop (AL) of the α -subunit and a significant N-terminal part of the β -subunit. **A**, domain organization of the *S. cerevisiae* AMPK ortholog. Snf1, Sip2, and Snf4 correspond to α -, β -, and γ -subunits, respectively, of mammalian AMPK (amino acid numbering according to *S. cerevisiae*, modified using Ref. 44). **B**, structural model of a putative full-length AMPK complex. The structure of the core complex of the *S. cerevisiae* AMPK ortholog (PDB 2QLV) is turned sidewise by 90° relative to the representations in Amodio *et al.* (44). Three AMP molecules (one fixed, two exchangeable) were introduced by superposition with the very homologous core structures of mammalian AMPK using PDB 2V8Q (see also supplemental Fig. 1). The α -subunit KD (Protein Data Bank code 2H6D) was added to its putative location (see Fig. 1B in Ref. 43), in close proximity to the α -subunit RS and with the active site pointing to the outside of the complex. Some part of the RS, including the autoinhibitory domain with a conserved putative α -helix, is not resolved in any of the known x-ray structures. The autoinhibitory domain was proposed to bind to the backside of the small lobe of the KD (72). Note: the RS is sandwiched between the γ -subunit (*blue*), with its AMP binding sites, and the KD (*gray*). This would allow the RS to mediate a cross-talk between AMP binding sites and the KD or other parts of the AMPK complex as outlined in C. **C**, simplified model for the mechanism of AMPK regulation by AMP. This model is based on the putative structure of AMPK (shown in B) and incorporates data from us (this work and Ref. 10), as well as others (e.g. Refs. 43 and 72). The (P) in the KD indicates the activatory phosphorylation at Thr¹⁷² (6–9). *Left*, at the low AMP/ATP ratio, binding sites 1 and 2 are occupied by ATP and site 3 by non-exchangeable AMP. The Thr¹⁷²-phosphate group is easily accessible to protein phosphatase 2C α for dephosphorylation (10, 19), resulting in low AMPK activity. *Right*, at an increasing AMP/ATP ratio, replacement of ATP by AMP at reversible AMP-binding sites 1 and/or 2 would result in small conformational changes and/or changes in surface potential of the γ -subunit (43). Given the structure outlined in B, our model proposes transmission and amplification of these changes by the neighboring RS and KD (*small open arrows*) leading to release of autoinhibition of the KD by retracting the RS and pulling the KD closer to the core of the AMPK molecule. The overall compaction of the heterotrimer is interpreted in our model as a movement of RS (*red arrow*) and KD (*black arrow*), as well as a conformational change in the KD. The latter would protect phospho-Thr¹⁷² against dephosphorylation, thus keeping AMPK in its phosphorylated, active form.

sentation as published in Amodio *et al.* (44) (Fig. 9B and supplemental Fig. S1) by 90°, it is obvious that one exchangeable AMP-binding site (site 1) in the γ -subunit (Fig. 9B, *blue*) is very close to the regulatory sequence of the α -subunit (Fig. 9B, *RS red*). The second AMP-binding site (site 2) and the site containing a non-exchangeable, fixed AMP (site 3) are somewhat more distant to the RS. Furthermore, the x-ray structure of the isolated AMPK kinase domain (Protein Data Bank code 2H6D) was positioned with the active site pointing to the outside of the complex (Fig. 9B, *gray*). From this topology it is obvious that the RS together with a neighboring sequence, which are missing in the crystallized structures (including a putative regulatory helix

suggested by Pang and colleagues (72)), are sandwiched between the γ -subunit and the α -subunit kinase domain. It is thus entirely conceivable that a small conformational change and/or a change in the γ -subunit surface charge upon AMP binding (as in the *S. pombe* x-ray structure, see Fig. 2, D and F, in Ref. 43) could be transmitted via the RS onto the kinase domain and possibly other domains of AMPK (Fig. 9C). Involvement of the β -subunit Ser¹⁰⁸ autophosphorylation site in activation of AMPK has been reported recently (73), suggesting that the β -subunit may also come close to the kinase domain, consistent with our model (Fig. 9, B and C). These effects would finally lead to the overall conformational change of the AMPK molecule as observed by SAXS in this work. According to this conformational switch model, the RS would not act as an autoinhibitory pseudosubstrate sequence inside the kinase domain loop, as for example in PKA and other protein kinases (see Ref. 72), but rather contact the kinase domain at its backside. Upon AMP binding to the γ -subunit, the RS relocates and thereby releases autoinhibition (Fig. 9C). Please note that the structural part of the RS, which supposedly would associate with the kinase domain, is not resolved in any of the published AMPK x-ray structures and thus structural information is not included in Fig. 9B.

Our model proposes that changes induced by AMP binding in the γ -subunit and transmitted via the RS sequence to the α -subunit may also alter accessibility of the phospho-Thr¹⁷² residue. This would make it less susceptible for dephosphorylation by protein phosphatase 2C α (10, 19), thus prolonging AMPK activation in the presence of AMP (Fig. 9C). The entire process of AMP sensing and transmission of the conformational changes would lead to an overall compacting of the AMPK molecule as shown by SAXS (Figs. 5 and 6) and depicted schematically in our model (Fig. 9C). The model integrating many old and recent findings seems consistent with published data and may give some new clues for further studies on the allosteric activation of AMPK.

Taken together, the quantitative results presented here shed new light on the molecular shape of native AMPK heterotrimer, at the resolution attainable by negative stain TEM methods and

in-solution SAXS techniques. Overall, the molecular shape of AMPK particles was consistent, irrespective of the method applied, suggesting that it reflects the “true” structural/functional state of mammalian AMPK at this resolution. The studies revealed a rapid concentration-dependent equilibrium between AMPK heterotrimers and defined dimers thereof. Finally, and most importantly, an AMP-induced conformational switch is shown in the full-length AMPK complex, suggesting a molecular mechanism for AMPK activation by allosteric activators. The techniques and results developed herein are expected to stimulate new and original approaches to pursue high-resolution structural characterization of full-length AMPK, as well as to aid a more detailed study of AMPK regulation *in vivo*.

Acknowledgments—We thank Ulrich Bauer (former Institute of Biotechnology, ETH Zurich) for introducing U. R. to the art of running large bioreactors, Marco Gregorini (M. E. Müller Institute for Structural Biology, Basel) for contributions to TEM microscopy, and Saccinthe Ramirez (Inserm U884/LBFA, UJF Grenoble) for assistance during the SAXS measurements at DESY, Hamburg. All members of the Wallimann group are acknowledged for help and discussions.

REFERENCES

- Kahn, B. B., Alquier, T., Carling, D., and Hardie, D. G. (2005) *Cell Metab.* **1**, 15–25
- Hardie, D. G. (2007) *Nat. Rev. Mol. Cell Biol.* **8**, 774–785
- Carling, D. (2005) *Biochimie (Paris)* **87**, 87–91
- Lee, J. H., Koh, H., Kim, M., Kim, Y., Lee, S. Y., Karess, R. E., Lee, S. H., Shong, M., Kim, J. M., Kim, J., and Chung, J. (2007) *Nature* **447**, 1017–1020
- Neumann, D., Wallimann, T., Rider, M., Tokarska-Schlattner, M., Hardie, D. G., and Schlattner, U. (2007) in *Molecular System Bioenergetics, Energy for Life* (Saks, V., ed) 1st Ed., pp. 303–338, Wiley-VCH, Weinheim, Germany
- Hawley, S. A., Boudeau, J., Reid, J. L., Mustard, K. J., Udd, L., Makela, T. P., Alessi, D. R., and Hardie, D. G. (2003) *J. Biol.* **2**, 28
- Shaw, R. J., Kosmatka, M., Bardeesy, N., Hurley, R. L., Witters, L. A., DePinho, R. A., and Cantley, L. C. (2004) *Proc. Natl. Acad. Sci. U. S. A.* **101**, 3329–3335
- Woods, A., Johnstone, S. R., Dickerson, K., Leiper, F. C., Fryer, L. G., Neumann, D., Schlattner, U., Wallimann, T., Carlson, M., and Carling, D. (2003) *Curr. Biol.* **13**, 2004–2008
- Hawley, S. A., Pan, D. A., Mustard, K. J., Ross, L., Bain, J., Edelman, A. M., Frenguelli, B. G., and Hardie, D. G. (2005) *Cell Metab.* **2**, 9–19
- Suter, M., Riek, U., Tuerk, R., Schlattner, U., Wallimann, T., and Neumann, D. (2006) *J. Biol. Chem.* **281**, 32207–32216
- Hardie, D. G., and Carling, D. (1997) *Eur. J. Biochem.* **246**, 259–273
- Scott, J. W., Hawley, S. A., Green, K. A., Anis, M., Stewart, G., Scullion, G. A., Norman, D. G., and Hardie, D. G. (2004) *J. Clin. Investig.* **113**, 274–284
- Hardie, D. G., Hawley, S. A., and Scott, J. W. (2006) *J. Physiol.* **574**, 7–15
- Xiao, B., Heath, R., Saiu, P., Leiper, F. C., Leone, P., Jing, C., Walker, P. A., Haire, L., Eccleston, J. F., Davis, C. T., Martin, S. R., Carling, D., and Gambelin, S. J. (2007) *Nature* **449**, 496–500
- McGilvery, R., and Murray, T. W. (1974) *J. Biol. Chem.* **249**, 5845–5850
- Hardie, D. G., and Hawley, S. A. (2001) *Bioessays* **23**, 1112–1119
- Neumann, D., Schlattner, U., and Wallimann, T. (2003) *Biochem. Soc. Trans.* **31**, 169–174
- Schlattner, U., and Wallimann, T. (2004) in *Encyclopedia of Biological Chemistry* (Lennarz, W. J., and Lane, M. D., eds) pp. 646–651, Academic Press, New York
- Sanders, M. J., Grondin, P. O., Hegarty, B. D., Snowden, M. A., and Carling, D. (2007) *Biochem. J.* **403**, 139–148
- Iseli, T. J., Walter, M., van Denderen, B. J., Katsis, F., Witters, L. A., Kemp, B. E., Michell, B. J., and Stapleton, D. (2005) *J. Biol. Chem.* **280**, 13395–13400
- Wong, K. A., and Lodish, H. F. (2006) *J. Biol. Chem.* **281**, 36434–36442
- Hudson, E. R., Pan, D. A., James, J., Lucocq, J. M., Hawley, S. A., Green, K. A., Baba, O., Terashima, T., and Hardie, D. G. (2003) *Curr. Biol.* **13**, 861–866
- Polekhina, G., Gupta, A., Michell, B. J., van Denderen, B., Murthy, S., Feil, S. C., Jennings, I. G., Campbell, D. J., Witters, L. A., Parker, M. W., Kemp, B. E., and Stapleton, D. (2003) *Curr. Biol.* **13**, 867–871
- Warden, S. M., Richardson, C., O'Donnell, J., Jr., Stapleton, D., Kemp, B. E., and Witters, L. A. (2001) *Biochem. J.* **354**, 275–283
- Hardie, D. G., and Sakamoto, K. (2006) *Physiol. (Bethesda)* **21**, 48–60
- Minokoshi, Y., Kim, Y. B., Peroni, O. D., Fryer, L. G., Muller, C., Carling, D., and Kahn, B. B. (2002) *Nature* **415**, 339–343
- Ruderman, N. B., Saha, A. K., and Kraegen, E. W. (2003) *Endocrinology* **144**, 5166–5171
- Hardie, D. G. (2005) *Curr. Opin. Cell Biol.* **17**, 167–173
- Carretero, J., Medina, P. P., Blanco, R., Smit, L., Tang, M., Roncador, G., Maestre, L., Conde, E., Lopez-Rios, F., Clevers, H. C., and Sanchez-Cespedes, M. (2007) *Oncogene* **26**, 1616–1625
- Andersson, Y., Le, H., Juell, S., and Fodstad, O. (2006) *Mol. Cancer Ther.* **5**, 1050–1059
- Ashrafian, H. (2006) *Lancet* **367**, 618–621
- Luo, Z., Saha, A. K., Xiang, X., and Ruderman, N. B. (2005) *Trends Pharmacol. Sci.* **26**, 69–76
- Bolster, D. R., Crozier, S. J., Kimball, S. R., and Jefferson, L. S. (2002) *J. Biol. Chem.* **277**, 23977–23980
- Dolinsky, V. W., and Dyck, J. R. (2006) *Am. J. Physiol.* **291**, H2557–H2569
- Davies, J. K., Wells, D. J., Liu, K., Whitrow, H. R., Daniel, T. D., Grignani, R., Lygate, C. A., Schneider, J. E., Noel, G., Watkins, H., and Carling, D. (2006) *Am. J. Physiol.* **290**, H1942–H1951
- Gollob, M. H. (2003) *Biochem. Soc. Trans.* **31**, 228–231
- Hardie, D. G. (2007) *Annu. Rev. Pharmacol. Toxicol.* **47**, 185–210
- Rudolph, M. J., Amodeo, G. A., Bai, Y., and Tong, L. (2005) *Biochem. Biophys. Res. Commun.* **337**, 1224–1228
- Nayak, V., Zhao, K., Wyce, A., Schwartz, M. F., Lo, W. S., Berger, S. L., and Marmorstein, R. (2006) *Structure* **14**, 477–485
- Polekhina, G., Feil, S. C., Gupta, A., O'Donnell, P., Stapleton, D., and Parker, M. W. (2005) *Acta Crystallogr. Sect. F Struct. Biol. Crystallogr. Commun.* **61**, 39–42
- Rudolph, M. J., Amodeo, G. A., Iram, S. H., Hong, S. P., Pirino, G., Carlson, M., and Tong, L. (2007) *Structure* **15**, 65–74
- Day, P., Sharff, A., Parra, L., Cleasby, A., Williams, M., Horer, S., Nar, H., Redemann, N., Tickle, I., and Yon, J. (2007) *Acta Crystallogr. D Biol. Crystallogr.* **63**, 587–596
- Townley, R., and Shapiro, L. (2007) *Science* **315**, 1726–1729
- Amodeo, G. A., Rudolph, M. J., and Tong, L. (2007) *Nature* **449**, 492–495
- Neumann, D., Woods, A., Carling, D., Wallimann, T., and Schlattner, U. (2003) *Protein Expression Purif.* **30**, 230–237
- Riek, U., Tuerk, R., Wallimann, T., Schlattner, U., and Neumann, D. (2008) *Biotechniques* (in press)
- Neumann, D., Suter, M., Tuerk, R., Riek, U., and Wallimann, T. (2007) *Mol. Biotechnol.* **36**, 220–231
- Müller, S. A., Goldie, K. N., Bürki, R., Häring, R., and Engel, A. (1992) *Ultramicroscopy* **46**, 317–334
- Müller, S. A., and Engel, A. (2001) *Micron* **32**, 21–31
- Ludtke, S. J., Baldwin, P. R., and Chiu, W. (1999) *J. Struct. Biol.* **128**, 82–97
- Nazabal, A., Wenzel, J. R., and Zenobi, R. (2006) *Anal. Chem.* **78**, 3562–3570
- Boulin, C. J., Kempf, R., Gabriel, A., and Koch, M. H. J. (1988) *Nucl. Instrum. Meth. A* **269**, 312–320
- Roessle, M. W., Klaering, R., Ristau, U., Robrahn, B., Jahn, D., Gehrman, T., Konarev, P., Round, A., Fiedler, S., Hermes, C., and Svergun, D. (2007) *J. Appl. Crystallogr.* **40**, 190–194
- Konarev, P. V., Volkov, V. V., Sokolova, A. V., Koch, M. H. J., and Svergun, D. I. (2003) *J. Appl. Crystallogr.* **36**, 1277–1282

55. Konarev, P. V., Petoukhov, M. V., Volkov, V. V., and Svergun, D. I. (2006) *J. Appl. Crystallogr.* **39**, 227–286
56. Guinier, A., and Fournet, G. (1955) *Small Angle Scattering of X-rays*, Wiley, New York
57. Svergun, D. I. (1992) *J. Appl. Crystallogr.* **25**, 495–503
58. Porod, G. (1982) in *Small-angle X-ray Scattering* (Glatter, O., and Kratky, O., eds) pp. 17–51, Academic Press, London
59. Svergun, D. I. (1999) *Biophys. J.* **76**, 2879–2886
60. Volkov, V. V., and Svergun, D. I. (2003) *J. Appl. Crystallogr.* **36**, 860–864
61. Treebak, J. T., Glund, S., Deshmukh, A., Klein, D. K., Long, Y. C., Jensen, T. E., Jorgensen, S. B., Viollet, B., Andersson, L., Neumann, D., Wallimann, T., Richter, E. A., Chibalin, A. V., Zierath, J. R., and Wojtaszewski, J. F. (2006) *Diabetes* **55**, 2051–2058
62. Xie, Z., Dong, Y., Zhang, M., Cui, M. Z., Cohen, R. A., Riek, U., Neumann, D., Schlattner, U., and Zou, M. H. (2006) *J. Biol. Chem.* **281**, 6366–6375
63. Horman, S., Vertommen, D., Heath, R., Neumann, D., Mouton, V., Woods, A., Schlattner, U., Wallimann, T., Carling, D., Hue, L., and Rider, M. H. (2006) *J. Biol. Chem.* **281**, 5335–5340
64. Baron, S. J., Li, J., Russell, R. R., 3rd, Neumann, D., Miller, E. J., Tuerk, R., Wallimann, T., Hurley, R. L., Witters, L. A., and Young, L. H. (2005) *Circ. Res.* **96**, 337–345
65. Carattino, M. D., Edinger, R. S., Grieser, H. J., Wise, R., Neumann, D., Schlattner, U., Johnson, J. P., Kleyman, T. R., and Hallows, K. R. (2005) *J. Biol. Chem.* **280**, 17608–17616
66. Zou, M. H., Kirkpatrick, S. S., Davis, B. J., Nelson, J. S., Wiles, W. G., 4th, Schlattner, U., Neumann, D., Brownlee, M., Freeman, M. B., and Goldman, M. H. (2004) *J. Biol. Chem.* **279**, 43940–43951
67. Taylor, E. B., Ellingson, W. J., Lamb, J. D., Chesser, D. G., Compton, C. L., and Winder, W. W. (2006) *Am. J. Physiol.* **290**, E661–E669
68. Taylor, E. B., Ellingson, W. J., Lamb, J. D., Chesser, D. G., and Winder, W. W. (2005) *Am. J. Physiol.* **288**, E1055–E1061
69. Svergun, D. I., Barberato, C., and Koch, M. H. J. (1995) *J. Appl. Crystallogr.* **28**, 768–773
70. Elbing, K., Rubenstein, E. M., McCartney, R. R., and Schmidt, M. C. (2006) *J. Biol. Chem.* **281**, 26170–26180
71. Mitchelhill, K. I., Michell, B. J., House, C. M., Stapleton, D., Dyck, J., Gamble, J., Ullrich, C., Witters, L. A., and Kemp, B. E. (1997) *J. Biol. Chem.* **272**, 24475–24479
72. Pang, T., Xiong, B., Li, J. Y., Qiu, B. Y., Jin, G. Z., Shen, J. K., and Li, J. (2007) *J. Biol. Chem.* **282**, 495–506
73. Sanders, M. J., Ali, Z. S., Hegarty, B. D., Heath, R., Snowden, M. A., and Carling, D. (2007) *J. Biol. Chem.* **282**, 32539–32548